Supporting information for:

Resonant Inelastic X-ray Scattering on Ferrous and Ferric bis-imidazole Porphyrin and Cytochrome *c*: Nature and Role of the Axial Methionine – Fe Bond

Thomas Kroll,[†,‡] Ryan G. Hadt,[†] Samuel A. Wilson,[†] Marcus Lundberg,[†,¶] James J. Yan,[†] Tsu-Chien Weng,[§] Dimosthenis Sokaras,[§] Roberto Alonso-Mori,[‡] Diego Casa,[‖] Mary H. Upton,[‖] Britt Hedman,[*,§] Keith O. Hodgson,[*,†,§] and Edward I. Solomon[*,†,§]

Department of Chemistry, Stanford University, Stanford, CA 94305, USA, Linac Coherent Light Source, SLAC National Accelerator Laboratory, Stanford University, Menlo Park, CA 94025, USA, Department of Chemistry - Ångström, Uppsala University, SE-751 20 Uppsala, Sweden, Stanford Synchrotron Radiation Lightsource, SLAC National Accelerator Laboratory, Stanford University, Menlo Park, CA 94025, USA, and Advanced Photon Source, Argonne National Laboratory, 9700 South Cass Avenue, Argonne, IL 60439, USA

E-mail: hedman@slac.stanford.edu; hodgson@slac.stanford.edu; edward.solomon@stanford.edu

[*]To whom correspondence should be addressed
[†]Stanford University
[‡]LCLS
[¶]Uppsala University
[§]SSRL
[‖]APS

Introduction

Different Molecular structures have been used for DFT calculations of the electronic structure for both ferrous and ferric cases. The structures used for $FeTPP(ImH)_2$, cyt *c*, and the truncated models are shown in Figure S1.

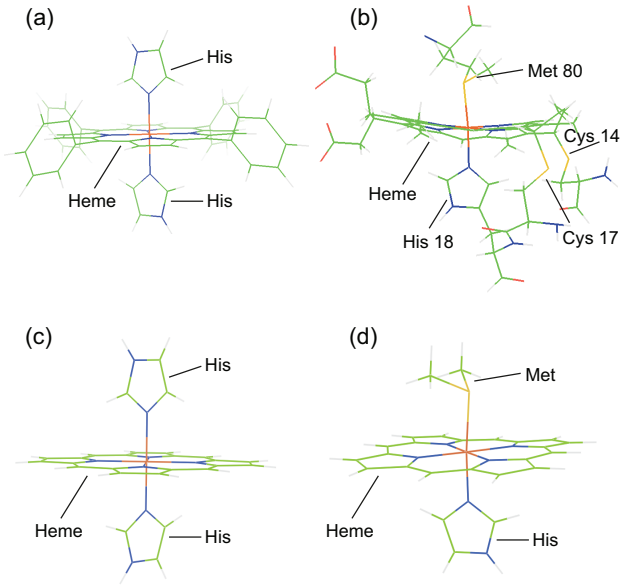

Figure S1: Molecular structures of (a) $FeTPP(ImH)_2$, (b) its counterpart inside cyt *c*, and the truncated models having (c) bis-His and (d) Met-His axial ligands.

Sample Preparation

Ferrous and ferric $FeTPP(ImH)_2$: All chemicals were obtained from Sigma-Aldrich Co. as the highest purity available and were used without further purification unless otherwise indicated. Anaerobic preparations were done in a nitrogen glove box using anhydrous solvents that were degassed by 5 freeze-pump-thaw cycles under an argon atmosphere.

$[Fe^{III}(tpp)(ImH)_2]Cl$ (tpp = *5,10,15,20-tetraphenyl-21H,23H*-porphine, ImH = imidazole) was synthesized according to published methods.[S1] 500 mg (0.71 mmol) of Fe(tpp)Cl was mixed with 6 equivalents of imidazole in 60 mL of chloroform. A suitable product for analysis was obtained through the slow addition using hexane or by crystallization by hexane

diffusion.

$[Fe^{II}(tpp)(ImH)_2]$ was prepared under an anaerobic atmosphere by direct reduction with excess sodium borohydride ($NaBH_4$). According to the procedure of Mink *et al.*[S2] 100 mg (0.14 mmol) of Fe(tpp)Cl was dissolved in 50 ml of tetrahydrofuran (THF) and reduced using a 100 fold excess (14.2 mmol) of $NaBH_4$, which turned the solution from brown to red. The reaction was monitored by UV-vis absorption to ensure the complete reduction of Fe^{III} to Fe^{II}. After 48 hours, 12 equivalents (1.70 mmol) of imidazole were added and the reaction was stirred for 30 minutes, after which the solvent was removed under reduced pressure to yield a product suitable for XAS.

Reduced and oxidized cytochrome *c*: Horse heart cyt *c* (type IV) was obtained from Sigma (>95% purity, SDS-page). The protein was further purified using cation exchange chromatography and an ÄKTApurifier UPC 100 manufactured by GE Healthcare Life Sciences. Samples were buffer exchanged into 100 mM phosphate buffer, pH 6.8, and concentrated to ∼4 mM. Reduction of cyt *c* samples was performed by anaerobic addition of aliquots of sodium dithionite ($Na_2S_2O_4$). Protein samples were injected into Lucite cells with Kapton windows and immediately frozen and stored under liquid nitrogen.

Experimental Methods

L-edge X-ray absorption spectra were recorded at the Stanford Synchrotron Radiation Lightsource (SSRL) on the undulator beam line 10-1 under ring operating conditions of 350 mA and 3 GeV. The radiation was dispersed using a spherical grating monochromator set at 1000 lines/mm and 20 μm entrance and exit slits (0.15 eV resolution). All measurements were done at a sample temperature of around 240 K. Measurements were performed using the total electron yield mode, where the sample signal was collected using a Galileo 4716 channeltron electron multiplier aligned 45° relative to the sample surface normal, which was aligned parallel to the incident beam. The signal was flux normalized by the photocurrent

of a gold-grid reference monitor. Data for all samples were recorded in a sample chamber maintained at $\approx 3 \times 10^{-9}$ Torr. The photon energy was calibrated using the Fe L-edge XAS of powdered R-Fe_2O_3 (hematite) run at intervals between scans. The second feature in the L_3-edge and the first feature in the L_2-edge were calibrated to 708.5 and 720.1 eV, respectively. Samples were finely ground and spread across double-sided adhesive conductive graphite tape attached to a copper sample holder aligned at 45° to the incident beam. Data were taken over the range 670-830 eV to permit normalization, as described previously.[S3,S4] No photo-damage was observed during one run in any of the samples described herein.

K-edge Ferrous and ferric $FeTPP(ImH)_2$ sample were mixed with boron nitride and ground into a fine powder. The powder was loaded into a 1 mm thick Al spacer and sealed with 63.5 μm Kapton tape windows. Fe K-edges were measured in transition mode with N_2-filled ionization chambers at SSRL beam line 7-3. Two or three scans were measured per sample to ensure reproducibility. Energies were calibrated against the first inflection point at 7111.2 eV of an internal foil standard.[S5] A second-order polynomial was fit to the pre-edge and subtracted from the data. A two-segment spline of order 2 was fit to the EXAFS region, and all data were normalized to the edge jump at 7130 eV.

1s2p RIXS *Data collection:* 1s2p RIXS experiments were carried out at SSRL beam line 6-2[S6] and APS beam line 9-ID.[S7,S8] They are equipped with a liquid nitrogen cooled double-crystal monochromator (Si(1,1,1) and Si(3,1,1)), allowing for high resolution of the incoming radiation (≈0.2 eV) in the energy range of 7100-7300 eV. The (440) Bragg reflection of five (SSRL) and one (APS) Ge(110) crystals arranged in a 1m Rowland geometry were used to select the K_α emission energy. A single element silicon drift detector (SSRL) and a line detector (APS) were used to measure the X-ray emission. The emitted beam path was enclosed by a He-filled bag to reduce the signal attenuation at SSRL. The total resolution was ≈0.6 (SSRL) and ≈0.5 eV (APS), which is sufficient for a detailed analysis. To reduce photo-damage, a liquid He cooled cryostat for measurements at 10 K was used, as well as

a sample stage that is equipped with motors to allow for horizontal and vertical movement for multiple sampling positions. Energies were calibrated against the first inflection point at 7111.2 eV of an internal foil standard.[S5] The RIXS plane was recorded by scanning the incident energy in a step-wise mode at fixed emission energy.

Only oxidized cyt *c* was sensitive to photo-reduction under X-ray irradiation. The effects of photo-damage was excluded by minimizing the count time and shortening the incident energy scan region, in addition to movement of the sample stage for each emission energy. To get a reasonable signal-to-noise ratio, the 1s2p RIXS plane was measured four times and summed.

Rising-edge subtraction: The pre-edge in a 1s2p RIXS experiment suffers from the tail of the intense $1s \rightarrow 4p$ excitations at around 15 eV higher energy. This leads to an increase of the pre-edge background and further complicates a direct comparison of L-edge data with constant incident energy (CIE, i.e. vertical) cuts through the RIXS plane. Furthermore, it overlaps with intensity contributions due to π back-bonding. In order to estimate the intensity from the tail of the rising-edge, the RIXS data were fit and the resulting background subtracted. To fit the experimental data, up to 15 Pearson VII functions depending on the complexity of the pre-edge and edge structure were fitted to each horizontal cut, separated into an resonant (pre-edge) and non-resonant (rising-edge) region. The main difference between the two regions is the shift in peak position when increasing the incident energy: For resonant excitations, no shift is expected, while for non-resonant excitations, a shift in energy of the size of the incident energy step is expected. These constrains have been incorporated in the fits. An example is given in Figure S2. For further details see Ref.[S9]

All data sets (L-edge, K-edge, 1s2p RIXS) have been measured at minimum twice to ensure reproducible and reliable data.

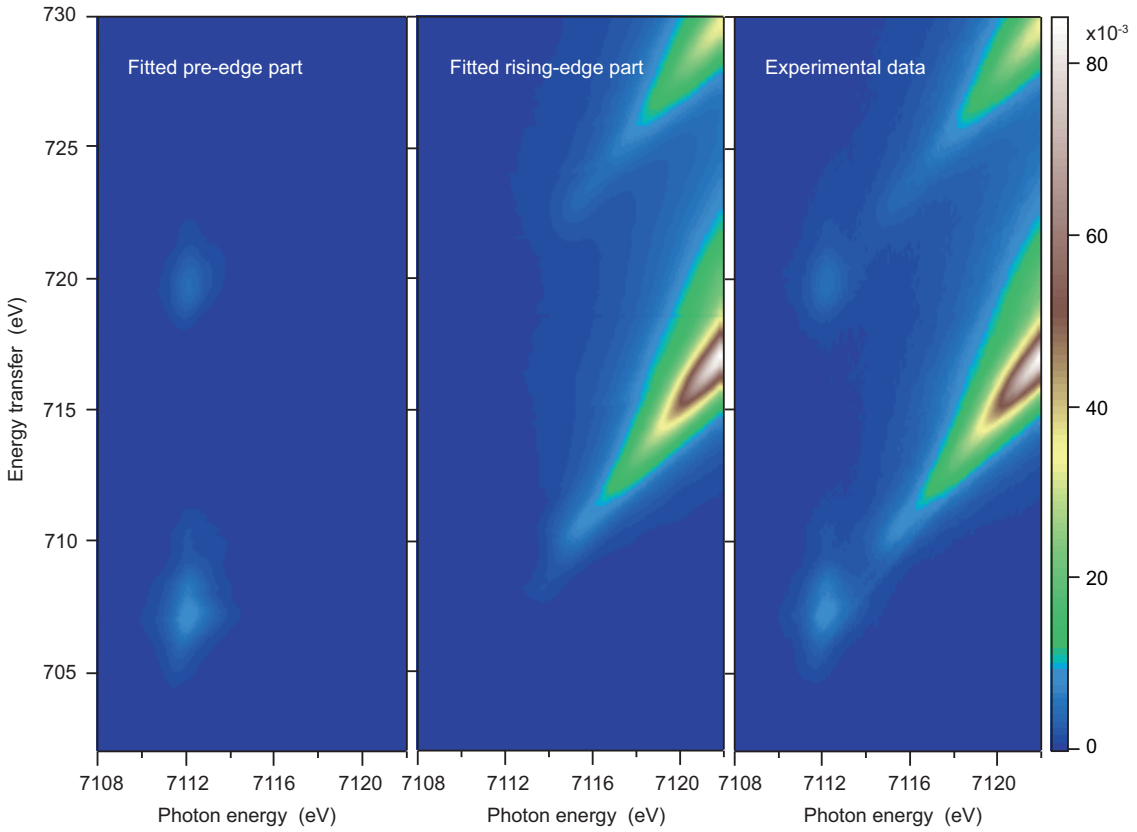

Figure S2: 1s2p RIXS plane fit result of Fe(II)TPP(ImH)$_2$. Left and Middle: Resulting pre-edge and edge fit result, respectively, from a fit to the full RIXS plane. Right: Experimental RIXS plane.

Computational Details

Multiplet Calculations Charge transfer multiplet calculations were performed using the atomic theory developed by Cowan[S10] and the crystal field interactions described by Butler,[S11] including electronic Coulomb interactions and spin-orbit coupling for each subshell.[S12–S14] The Slater-Condon-Shortley parameters F_i and G_i were reduced from their Hartree-Fock calculated values to account for the over-estimation of electron-electron repulsion found in the calculations of the free ion.[S12,S15,S16] Covalent mixing of ligand character is modeled in the simulations using a valence bond configuration interaction (VBCI) model as implemented by Thole.[S17] A three configuration model is employed that includes a ligand-to-metal charge transfer (LMCT) configuration $d^{n+1}\underline{L}$ and a metal-to-ligand charge transfer (MLCT) configuration $d^{n-1}L^{-}$ mixed into the d^n configuration in the ground state.

($\underline{L}$=ligand with an e^- hole, L^-=ligand with an additional e^- electron) The corresponding charge transfer energies Δ (LMCT) and Δ^* (MLCT) are defined as

$$\begin{aligned} \Delta &= E(d^{n+1}\underline{L}) - E(d^n) \text{ and} \\ \Delta^* &= E(d^{n-1}L^-) - E(d^n). \end{aligned} \quad (1)$$

The configuration interaction is represented by the mixing terms $T_i = \langle d^n|h|d^{n+1}\underline{L}\rangle$ and $T_i^* = \langle d^n|h^*|d^{n-1}L^-\rangle$, where h and h^* are the LMCT and MLCT mixing operators, respectively. Thus T_i and T_i^* are proportional to the ligand-metal and metal-ligand overlap for each of the i^{th} symmetry blocks.

T_i and T_i^* as well as Δ and Δ^* were kept constant in the ground and final states, giving final state configuration energy separations of $E(\underline{c}d^{n+2}\underline{L}) - E(\underline{c}d^{n+1}) = \Delta + U_{dd} - Q$ and $E(\underline{c}d^nL^-) - E(\underline{c}d^{n+1}) = \Delta^* - U_{dd} + Q$, where U_{dd} is the 3d-3d and Q is the core-hole Coulomb attraction. The 1s2p RIXS includes an intermediate state with a $1s$ core-hole. In our simulations, it was assumed that $Q_{sd} = Q_{pd}$. However, the $1s3d$ and $2p3d$ Coulomb and exchange interactions are very different and these differences were incorporated in the simulations. All calculations have been performed in D_{4h} symmetry for all four complexes.

The covalency value for each of the symmetry blocks was generated via the projection method[S3] leading to the differential orbital covalency (DOC).

The theoretical spectra have been broadened by a Gaussian to include the experimental broadening and a Lorentzian to account for the life-time broadening with values given by the various peak widths of the reference sample ferri-cyanide,[S18,S19] which were measured before each run. For the L-edge spectra we used values of 0.4 and 0.4 (0.8) eV for Gaussian and L_3 (L_2) Lorentzian FWHM broadening, respectively. In the 1s2p RIXS simulations, all transitions are broadened by a Gaussian for simplicity, with an intermediate energy life-time broadening of 1.2 eV and experimental broadening of 0.3 eV. Final state broadenings were 0.7 (L_2) and 0.3 eV (L_3) (all FWHM).

While the Kramers-Heisenberg scattering equation (Equation **??**) allows for interference effects between intermediate states.,[S20] this is not included in the present simulations. Its significance to 1s2p RIXS is system dependent,[S21] and simulations that did also include interference effects showed no improvement in the fit to the data.[S22]

DFT Calculations The starting structure for FeTPP(ImH)$_2$ was taken from the ferric complex crystal structure,[S1] while the starting structure for cyt *c* optimization employed the horse heart oxidized cyt *c* structure.[S23] Ground state DFT calculations and geometry optimizations were performed with Gaussian 09[S24] using the unrestricted functional BP86,[S25,S26] modified to include Hartree-Fock (HF) mixing of 10 and 20% with a triple-zeta (6-311G*) basis set on Fe, N and S, and a double-zeta (6-31G*) basis set on all other atoms. For energy calculations, a basis set of triple-zeta quality (6-311+G(d,p)) and a polarized continuum model ($\epsilon = 4.0$) were used in combination with a BP86+20% HF exchange-correlation functional. Full Mulliken populations and Mulliken fragment populations were analyzed using QMForge.[S27] Unoccupied metal d-character has been determined by subtracting the sum of their contribution to all occupied orbitals from 100%. The ligand donor character has been obtained from the occupied fragment orbital character summed over the unoccupied orbitals.

Results and Analysis - Additional Information

Ferrous Spectroscopy

Figure S3 overlayes the background corrected K-edges of O_h Fe(II)−tacn and D_{4h} Fe(II)TPP(ImH)$_2$. This comparison limits the $d_{x^2-y^2}/d_{z^2}$ energy splitting in D_{4h} Fe(II)TPP(ImH)$_2$ to maximum 0.4 eV. Its back-bonding contribution is clearly visible at 7115 eV visible.

Figure S4 shows the comparison of the high-resolution emission curves for *cyt c* (red) and Fe(II)TPP(ImH)$_2$ (blue). Both curves overlay at higher energies (a) as well as in the rising edge (c). The steep onset, which is visible at energies right above the π^* feature at

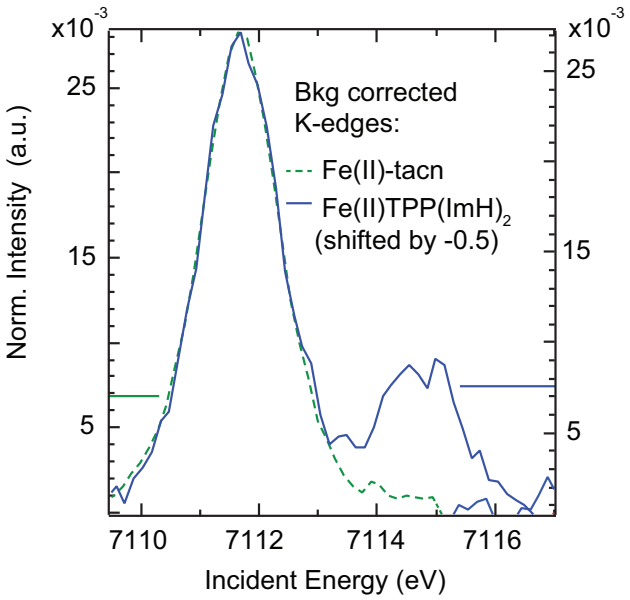

Figure S3: Comparison of the background corrected K-edges of O_h Fe(II) – tacn and D_{4h} Fe(II)TPP(ImH)$_2$. The identical width of the two K-edges limits the $d_{x^2-y^2}/d_{z^2}$ energy splitting to maximum 0.4 eV. Note that the additional peak for Fe(II)TPP(ImH)$_2$ at 7115 eV originates from π back-bonding, which is not present in Fe(II)-tacn.

7115.3 eV (b), thus originates either from multiplet scattering and/or shake down effects.

Ferrous multiplet simulations:

For Fe(II)TPP(ImH)$_2$ one can analyze both L-edge XAS and 1s2p RIXS, while only 1s2p RIXS is possible in cyt *c*. Comparing CEE and CIE cuts of both defines their quantitative difference. Thus charge-transfer multiplet calculations were performed within the VBCI framework. In a previous study, Fe(II)TPP(ImH)$_2$ has been simulated using the VBCI model to determine approximately 10% π back-bonding in the ground state wave function.[S4] A similar result was determined for the closely related ferrous picket-fence porphyrin complex.[S28] Here we follow these previous studies, but set the core-hole relaxation $U_{pd}-U_{dd}$ constant and treat both donation and back-bonding charge-transfer interactions as unchanged in ground and final states. The goal of these simulations is to first determine the parameter set that describes all the experimental results (K-edge, L-edge and 1s2p RIXS) for the reference

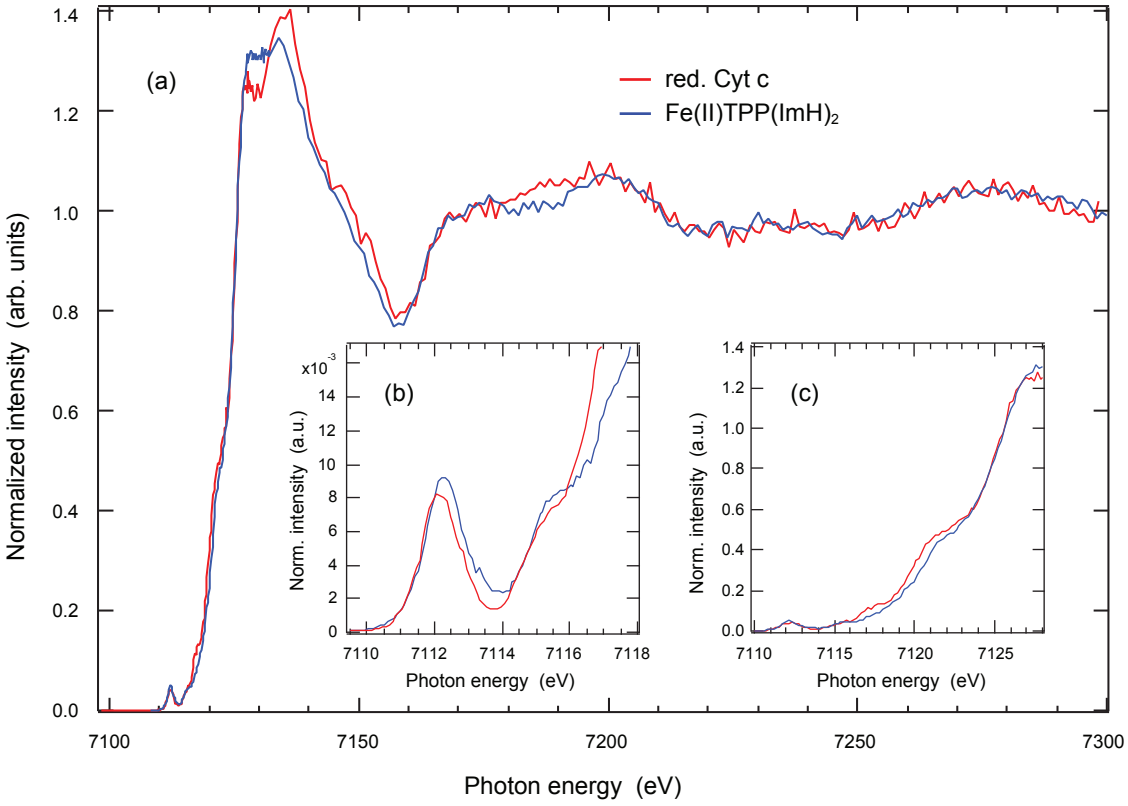

Figure S4: Comparison of the high resolution emission curves of *cyt c* and $Fe^{2+}TPP(ImH)_2$: (a) full curve, (b) pre-edge region, (c) pre- and rising-edge region.

$Fe(II)TPP(ImH)_2$ model complex, and then systematically evaluate parameter variations that reproduce the observed experimental changes in cyt *c*.

Accordingly, simulations of the reduced cyt *c* data were generated by starting from the simulation of the $Fe(II)TPP(ImH)_2$ model complex, and systematically varying the VBCI parameters to identify those that are responsible for the weak, but characteristic changes in the experimental spectral features between the cyt *c* and model complex spectra. The parameters used to simulate the spectra are given in Table S1.

Ferric multiplet simulations:

To simulate the oxidized cyt *c* data, the results of the $Fe(III)TPP(ImH)_2$ simulations were taken as a starting point, from which parameters were varied in a systematic manner to

Table S1: Collection of all parameter sets used to simulate all four complexes. Note that all MLCT mixing parameters are zero but T^*_{eg}, and $Q = Q_{sd} = Q_{pd}$. All values are in eV.

	crystal field			configuration energies			LMCT				MLCT
complexes	10Dq	Ds	Dt	Δ	Δ^*	Q-U	T_{b1g}	T_{a1g}	T_{eg}	T_{b2g}	T^*_{eg}
Fe(II)TPP(ImH)$_2$	2.5	0.02	0.04	1.3	0.6	1.0	1.8	1.5	1.5	0.5	0.7
ferrous cyt *c*	2.5	0.02	0.04	1.3	0.6	1.0	1.8	1.8	1.5	0.5	0.7
Fe(III)TPP(ImH)$_2$	3.0	-0.06	0.06	1.5	0.8	1.2	1.8	1.7	1.0	0.5	0.4
ferric cyt *c*	2.8	-0.06	0.06	1.5	0.8	1.2	1.8	1.9	1.2	0.5	0.4

reproduce all experimentally observed spectral changes.

Characteristic variations in the spectra were found to be associated with specific changes in the parameter set relative to Fe(III)TPP(ImH)$_2$. Similar to the ferrous case, an increase of the z^2 mixing parameter ($T_{a_{1g}}$) leads to an increase of the L_2-like intensity associated with σ excitation. However, an increase of $T_{a_{1g}}$ also leads to a shift to *higher* energies of the L_3-like peak (from σ excitation). To reproduce the shift to *lower* energies accompanied by the decrease in intensity of the L_3-like peak associated with π excitation, the mixing parameters for $d_{x^2-y^2}$ ($T_{b_{1g}}$) and $d_{xz/yz}$ (T_{e_g}) were increased, together with a decrease of the crystal field splitting $10Dq$.

Ligand Bond Strength:

In order to accurately calculate the axial ligand bond strengths, a DFT protocol was needed that reproduces the experimentally observed spin-states for both ligand-on and ligand-off forms. Several different exchange-correlation functionals were tested; the results are given in Tables S2-S5 (for BP86 with 0, 10, and 20 % HF admixtures (B(XXHF)P86), OPBE, OLYP, TPSSh, and B3LYP). Experimentally, the ligand-off state for Fe(II) in porphyrins and cyt *c* is high-spin, S = 2.[S29] This is reproduced with the B(20HF)P86, OPBE, OLYP, and B3LYP functionals (Table S2). Thus, the B(00HF)P86, B(10HF)P86, and TPSSh functionals were eliminated. The ligand-off state of Fe(III) in porphyrins and cyt *c* is typically intermediate-spin (S = 3/2) or a quantum admixture of intermediate- and high-spin (S=5/2) states.[S29–S32] The S = 3/2 ground state is reproduced by all functionals, but only the B(20HF)P86, OPBE, OLYP, and B3LYP functionals have the S = 5/2 state near enough in energy for quantum mixing (< 5 kcal/mol) (Table S3). Lastly, the ligand-on ground state for Fe(III)-S(Met) is low-spin, S = 1/2.[S29] The OPBE, OLYP, and B3LYP functionals predict the intermediate-spin S = 3/2 state to be lower in energy than the S=1/2 state (Table S4), while the B(20HF)P86 functional has the S = 1/2 and S = 3/2 states at similar energy, with the electronic energy (ΔE) and enthalpy (ΔH) giving the S=1/2 state lowest (Table S4). Thus, the B(20HF)P86 functional gives the best agreement between theory and experiment for both redox states and is used below. Note that all functionals predict similar trends in axial ligand bond strengths (Table S5). The B(20HF)P86 functional is also consistent with the 1s2p RIXS data and simulations as well as the DFT calculations for the large models.

Table S2: Relative energies of different spin-states for the Fe(II) N(His)/– (no axial ligand) models.[a,b]

Functional	ΔE	ΔH	ΔG
BP86 (0% HF)			
S=0	0.0	0.0	0.0
S=1	2.6	1.8	-0.6
S=2	15.3	14.0	10.0
BP86 (10% HF)			
S=0	2.5	3.1	5.5
S=1	0.0	0.0	0.0
S=2	6.2	5.5	4.1
BP86 (20% HF)			
S=0	6.4	6.9	9.3
S=1	0.0	0.0	0.0
S=2	0.3	-0.6	-1.9
OPBE			
S=0	5.1	6.2	9.3
S=1	0.0	0.0	0.0
S=2	0.5	0.3	-0.3
OLYP			
S=0	5.9	6.8	9.6
S=1	0.0	0.0	0.0
S=2	1.3	1.0	-0.6
TPSSh			
S=0	3.3	3.7	6.2
S=1	0.0	0.0	0.0
S=2	5.6	4.8	3.6
B3LYP			
S=0	6.8	7.2	9.6
S=1	0.0	0.0	0.0
S=2	0.6	-0.2	-1.7

[a] Energies are in kcal/mol and are reported as relative to the spin-state with the lowest electronic energy.
[b] Functionals that best reproduce experiment are bolded.

Table S3: Relative energies of different spin-states for the Fe(III) N(His)/– (no axial ligand) models.[a,b]

Functional	ΔE	ΔH	ΔG
BP86 (0% HF)			
S=1/2	2.7	2.8	4.0
S=3/2	0.0	0.0	0.0
S=5/2	16.3	15.3	14.1
BP86 (10% HF			
S=1/2	9.6	9.8	11.3
S=3/2	0.0	0.0	0.0
S=5/2	11.6	10.7	9.7
BP86 (20% HF)			
S=1/2	9.6	9.8	11.3
S=3/2	0.0	0.0	0.0
S=5/2	6.9	6.0	5.2
OPBE			
S=1/2	11.8	11.9	14.3
S=3/2	0.0	0.0	0.0
S=5/2	4.4	3.6	2.6
OLYP			
S=1/2	11.8	11.9	13.3
S=3/2	0.0	0.0	0.0
S=5/2	4.8	4.0	3.0
TPSSh			
S=1/2	4.7	4.1	6.3
S=3/2	0.0	0.0	0.0
S=5/2	9.9	9.0	8.1
B3LYP			
S=1/2	10.1	10.2	11.2
S=3/2	0.0	0.0	0.0
S=5/2	6.6	5.7	4.8

[a] Energies are in kcal/mol and are reported as relative to the spin-state with the lowest electronic energy.
[b] Functionals that best reproduce experiment are bolded.

Table S4: Relative energies of different spin-states for the Fe(III) N(His)/S(Met) (no axial ligand) models.[a,b]

Functional	ΔE	ΔH	ΔG
BP86 (0% HF)			
S=1/2	0.0	0.0	0.0
S=3/2	8.5	8.3	4.5
BP86 (10% HF			
S=1/2	0.0	0.0	0.0
S=3/2	4.6	4.2	0.5
BP86 (20% HF)			
S=1/2	0.0	0.0	0.0
S=3/2	1.2	0.7	-3.0
OPBE			
S=1/2	0.0	0.0	0.0
S=3/2	-6.4	-6.7	-13.9
OLYP			
S=1/2	0.0	0.0	0.0
S=3/2	-9.2	-9.6	-16.4
TPSSh			
S=1/2	0.0	0.0	0.0
S=3/2	5.6	5.1	1.6
B3LYP			
S=1/2	0.0	0.0	0.0
S=3/2	-1.8	-2.3	-6.7

[a] Energies are in kcal/mol and are reported as relative to the spin-state with the lowest electronic energy.
[b] Functionals that best reproduce experiment are bolded.

Table S5: Gas phase thermodynamics of Ligand Loss from $Fe^{II/III}$.

	Fe^{II}-S(Met)			Fe^{III}-S(Met)			Fe^{II}-N(His)			Fe^{III}-N(His))		
Functional	ΔE	ΔH	ΔG	ΔE	ΔH	ΔG	ΔE	ΔH	ΔG	ΔE	ΔH	ΔG
BP86 (0)	12.9	11.7	-1.2	13.9	12.6	-1.4	23.5	22.1	9.4	29.7	27.8	14.4
BP86 (10)	10.0	8.2	-7.0	10.8	9.2	-5.0	20.8	18.8	3.8	27.4	25.3	11.3
BP86(20)	5.5	3.9	-11.2	8.1	6.6 -	7.8	16.7	14.3	-0.4	25.4	23.3	9.1
OPBE*	-2.0	-4.4	-20.4	-4.3	-5.8	-19.7	7.1	4.5	-11.3	9.4	7.9	-8.0
OLYP*	-5.1	-7.3	-22.1	-6.9	-8.5	-22.3	5.5	3.1	-12.2	8.1	6.0	-7.5
TPSSh	9.5	8.0	-7.2	12.9	11.3	-3.0	20.8	19.0	3.8	30.0	28.0	13.7
B3LYP*	1.2	-0.4	-15.3	3.4	1.8	-12.4	12.9	11.1	-3.7	21.5	19.4	5.4

* Fe^{III}-S(Met), S = 3/2 lowest.

References

(S1) Scheidt, W. R.; Osvath, S. R.; Lee, Y. J. *Journal of the American Chemical Society* **1987**, *109*, 1958–1963.

(S2) Mink, L. M.; Polam, J. R.; Christensen, K. A.; Bruck, M. A.; Walker, F. A. *Journal of the American Chemical Society* **1995**, *117*, 9329–9339.

(S3) Wasinger, E. C.; de Groot, F. M. F.; Hedman, B.; Hodgson, K. O.; Solomon, E. I. *Journal of the American Chemical Society* **2003**, *125*, 12894–12906.

(S4) Hocking, R. K.; Wasinger, E. C.; Yan, Y.-L.; deGroot, F. M. F.; Walker, F. A.; Hodgson, K. O.; Hedman, B.; Solomon, E. I. *Journal of the American Chemical Society* **2007**, *129*, 113–125.

(S5) Scott, R. A.; Hahn, J. E.; Doniach, S.; Freeman, H. C.; Hodgson, K. O. *Journal of the American Chemical Society* **1982**, *104*, 5364–5369.

(S6) Sokaras, D.; Weng, T.-C.; Nordlund, D.; Alonso-Mori, R.; Velikov, P.; Wenger, D.; Garachtchenko, A.; George, M.; Borzenets, V.; Johnson, B.; Rabedeau, T.; Bergmann, U. *Review of Scientific Instruments* **2013**, *84*, 053102.

(S7) Gog, T.; Seidler, G. T.; Casa, D. M.; Upton, M. H.; Kim, J.; Stoupin, S.; Nagle, K. P.; Balasubramanian, M.; Gordon, R. A.; Fister, T. T.; Heald, S. M.; Toellner, T.; Hill, J. P.; Coburn, D. S.; Kim, Y.-J.; Said, A. H.; Alp, E. E.; Sturhahn, W.; Yavas, H.; Burns, C. A.; Sinn, H. *Synchrotron Radiation News* **2009**, *22*, 12–21.

(S8) Gog, T.; Casa, D. M.; Said, A. H.; Upton, M. H.; Kim, J.; Kuzmenko, I.; Huang, X.; Khachatryan, R. *Journal of Synchrotron Radiation* **2013**, *20*, 74–79.

(S9) Glatzel, P.; Bergmann, U.; Yano, J.; Visser, H.; Robblee, J. H.; Gu, W.; de Groot, F. M. F.; Christou, G.; Pecoraro, V. L.; Cramer, S. P.; Yachandra, V. K. *Journal of the American Chemical Society* **2004**, *126*, 9946–9959.

(S10) Cowan, R. D. *The Theory of Atomic Structure and Spectra*; University of California Press: Berkeley, 1981.

(S11) Butler, P. H. *Point Group Symmetry: Applications, Methods and Tables*; Plenum Press: New York, 1981.

(S12) Arrio, M.-A.; Sainctavit, P.; Cartier dit Moulin, C.; Mallah, T.; Verdaguer, M.; Pellegrin, E.; Chen, C. T. *Journal of the American Chemical Society* **1996**, *118*, 6422–6427.

(S13) van der Laan, G.; Kirkman, I. W. *Journal of Physics: Condensed Matter* **1992**, *4*, 4189–4204.

(S14) de Groot, F. M. F.; Kotani, A. *Core Level Spectroscopy of Solids*; CRC Press, Boca Raton, FL, 2008.

(S15) Arrio, M.-A.; Scuiller, A.; Sainctavit, P.; Cartier dit Moulin, C.; Mallah, T.; Verdaguer, M. *Journal of the American Chemical Society* **1999**, *121*, 6414–6420.

(S16) Cartier dit Moulin, C.; Villain, F.; Bleuzen, A.; Arrio, M.-A.; Sainctavit, P.; Lomenech, C.; Escax, V.; Baudelet, F.; Dartyge, E.; Gallet, J.-J.; Verdaguer, M. *Journal of the American Chemical Society* **2000**, *122*, 6653–6658.

(S17) Thole, B. T.; van der Laan, G.; C.Fuggle, J.; Sawatzky, G. A.; Karnatak, R. C.; Esteva, J.-M. *Physical Review B* **1985**, *32*, 5107–5118.

(S18) Hocking, R. K.; Wasinger, E. C.; de Groot, F. M. F.; Hodgson, K. O.; Hedman, B.; Solomon, E. I. *Journal of the American Chemical Society* **2006**, *128*, 10442–10451.

(S19) Lundberg, M.; Kroll, T.; DeBeer, S.; Bergmann, U.; Wilson, S. A.; Glatzel, P.; Nordlund, D.; Hedman, B.; Hodgson, K. O.; Solomon, E. I. *Journal of the American Chemical Society* **2013**, *135*, 17121–17134.

(S20) Gel'mukhanov, F.; Ögreen, H. *Physics Reports* **1999**, *312*, 87–330.

(S21) de Groot, F. M. F. *Physical Review B* **1996**, *53*, 7099–7110.

(S22) Kurian, R.; van Schooneveld, M. M.; Zoltán, N.; Vankó, G.; de Groot, F. M. F. *The Journal of Physical Chemistry C* **2013**, *117*, 2976–2981.

(S23) Bushnell, G. W.; Louie, G. V.; Brayer, G. D. *Journal of Molecular Biology* **1990**, *214*, 585 – 595.

(S24) Gaussian 09, Revision B.01,; Frisch, M. J.; Trucks, G. W.; Schlegel, H. B.; Scuseria, G. E.; Robb, M. A.; Cheeseman, J. R.; Scalmani, G.; Barone, V.; Mennucci, B.; Petersson, G. A.; Nakatsuji, H.; Caricato, M.; Li, X.; Hratchian, H. P.; Izmaylov, A. F.; Bloino, J.; Zheng, G.; Sonnenberg, J. L.; Hada, M.; Ehara, M.; Toyota, K.; Fukuda, R.; Hasegawa, J.; Ishida, M.; Nakajima, T.; Honda, Y.; Kitao, O.; Nakai, H.; Vreven, T.; Jr., J. A. M.; Peralta, J. E.; Ogliaro, F.; Bearpark, M.; Heyd, J. J.; Brothers, E.; Kudin, K. N.; Staroverov, V. N.; Kobayashi, R.; Normand, J.; Raghavachari, K.; Rendell, A.; Burant, J. C.; Iyengar, S. S.; Tomasi, J.; Cossi, M.; Rega, N.; Millam, J. M.; Klene, M.; Knox, J. E.; Cross, J. B.; Bakken, V.; Adamo, C.; Jaramillo, J.; Gomperts, R.; Stratmann, R. E.; Yazyev, O.; Austin, A. J.; Cammi, R.; Pomelli, C.; Ochterski, J. W.; Martin, R. L.; Morokuma, K.; Zakrzewski, V. G.; Voth, G. A.; Salvador, P.; Dannenberg, J. J.; Dapprich, S.; Daniels, A. D.; Farkas, Ö.; Foresman, J. B.; Ortiz, J. V.; Cioslowski, J.; Fox, D. J. Gaussian, Inc., Wallingford CT, 2009.

(S25) Becke, A. D. *Physical Review A* **1988**, *38*, 3098–3100.

(S26) Perdew, J. *Physical Review B* **1986**, *33*, 8822.

(S27) Tenderholt, A. L. QMForge: Tools for Converting the Output from QM Calculations into Something More Useful. 2014; `http://qmforge.sourceforge.net`.

(S28) Wilson, S. A.; Kroll, T.; Decreau, R. A.; Hocking, R. K.; Lundberg, M.; Hedman, B.; Hodgson, K. O.; Solomon, E. I. *Journal of the American Chemical Society* **2013**, *135*, 1124–1136.

(S29) Scheidt, W. R.; Reed, C. A. *Chemical Review* **1981**, *81*, 543–55.

(S30) Maltempo, M. M. *Journal of Chemical Physics* **1974**, *61*, 2540–7.

(S31) Weiss, R.; Gold, A.; Terner, J. *Chemical Review* **2006**, *106*, 2550–2579.

(S32) Reed, C. A.; Mashiko, T.; Bentley, S. P.; Kastner, M. E.; Scheidt, W. R.; Spartalian, K.; Lang, G. *Journal of the American Chemical Society* **1979**, *101*, 2948.